Chapter 6

A Versatile Plug-in Solution for Integrated Solar, Grid, and Vehicle Interactive Charging

6.1 Introduction

Global research on electric transportation highlights a significant rise in the popularity of EVs, driven by increasing environmental awareness. Electric vehicles on the road encompass a variety of types, including electric buses, sedans, and two- and three-wheeled vehicles such as rickshaws, autos, and trios. In Southeast Asia, three-wheelers play a crucial role in local transit systems. Since 2010, e-rickshaws have gained notable popularity in the Asian market due to their resemblance to traditional auto-rickshaws, making them a familiar and attractive alternative. Their appeal lies in the fact that they eliminate the need for constant pedaling throughout the day, unlike cycle rickshaws, leading to increased daily rides and greater profitability. According to a Bloomberg article, the collective number of electric three-wheeled rickshaws in South Asian countries has reached 1.5 million, surpassing the total sales of electric-powered passenger vehicles since 2011 in China. India and China stand out as the most prominent producers and consumers of EVs, followed by Thailand, as noted by Ward in 2018 [152]. According to an analyst, an estimated 60 million Indians use an EV daily [153]. The Asia-Pacific electric vehicle market

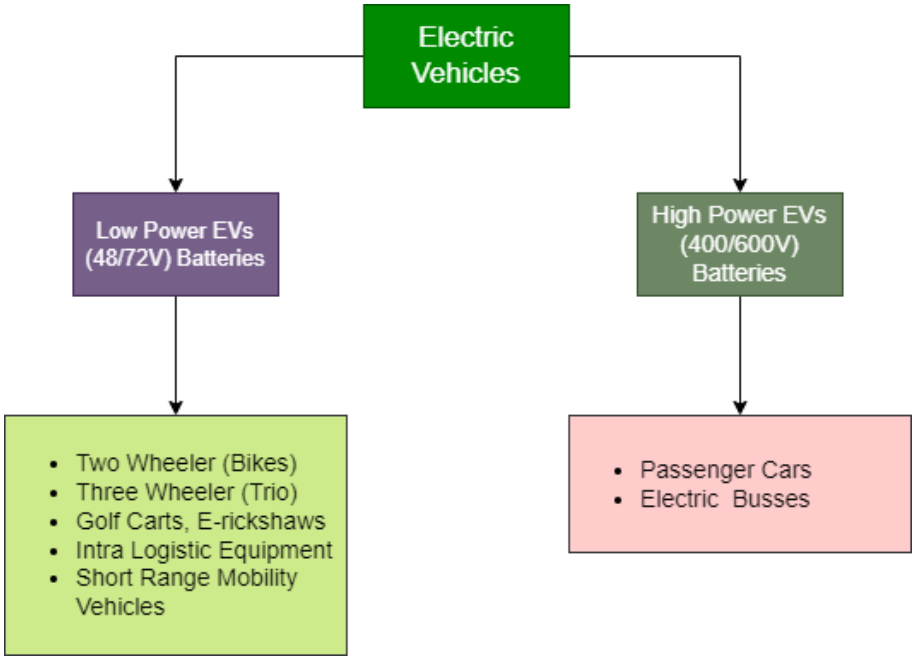

Figure 6.1: Classification of EVs.

is expected to grow at a 35% compound annual growth rate (CAGR) from 2022 to 2029, with an estimated value of $2,688.23$ billion by the end of 2029 [154]. The swift expansion of the electric vehicle market is largely driven by the cost-effectiveness of EVs, decreasing battery costs, and supportive government policies. According to forecasts from Policies and Support Intelligence, the Indian and Chinese markets are expected to double in size by 2024 [155].

Fig. 6.1 provides a visual representation of EV classification based on their battery capacity, while Table 6.1 outlines the various types of EV charging. Fig. 6.2 depicts the categorization of plug-in battery chargers for EVs. In this chapter, the present research introduces a non-isolated, multi-functional on-board charger for EVs to accommodate various charging needs. This innovative charger offers a comprehensive approach to charging, encompassing grid-based AC charging with power factor correction (PFC) through an AC-DC converter G2V, solar charging via interleaved buck-boost DC-DC converter S2V, and a unique emergency charge-sharing model in standalone mode among EVs (Vehicle-to-Vehicle, V2V). The focus of this study is on the analysis and design of a non-isolated buck-boost-derived PFC AC-DC converter for battery charging (G2V charging) operating in a simple discontinuous conduction mode (DCM). Configurations are meticulously examined and tailored for PFC op-

Table 6.1: EV Types and Charging Period.

EVs (Types)	**Battery (capacity)**	**Power (Charger)**	**Charging (Time)**
Two Wheeler/ three Wheeler	SLI - 48 (V)	0.5 - 1 kW	(6-8) hrs
Trio/ Golf Carts	Li-Ion / AGM 48V	1 -3 kW	(3-4) hrs
Range Mobility Vehicle	Li-Ion 120V	3.3 - 7 kW	4 hrs
public cars/ Buses	Li-Ion 400-600V	62 - 500 kW	30 mins

eration, employing a straightforward and effective control strategy. The interleaved operation reduces current stresses on semiconductor devices and minimizes input filter requirements, thereby enhancing the overall efficiency of the converter.

The proposed charger, compact in design, demonstrates flexibility in both conversion and control stages. Notably, this concept achieves and validates 1 kW operation with UPF at variable AC input, employing a small inductance, as evidenced by simulation results. In contrast to existing literature surveys, this chapter provides a unique perspective on the innovation and potential impact of the multifunctional plug-in EV battery charger in advancing sustainable transportation, supported by comprehensive simulation results. The subsequent sections delve into each charging mode's detailed design, operation, and performance evaluation, emphasizing this research's significance in sustainable and efficient EV charging systems.

Reducing total harmonic distortion (THD) is crucial for efficiency and minimizing interference in power systems, especially in applications like EV charging stations and PV inverters.THD is a parameter that evaluates the power quality in a power system network by measuring the presence of harmonic distortions. It can be calculated for current and voltage profiles, as demonstrated in equations 6.1 and 6.2, respectively.

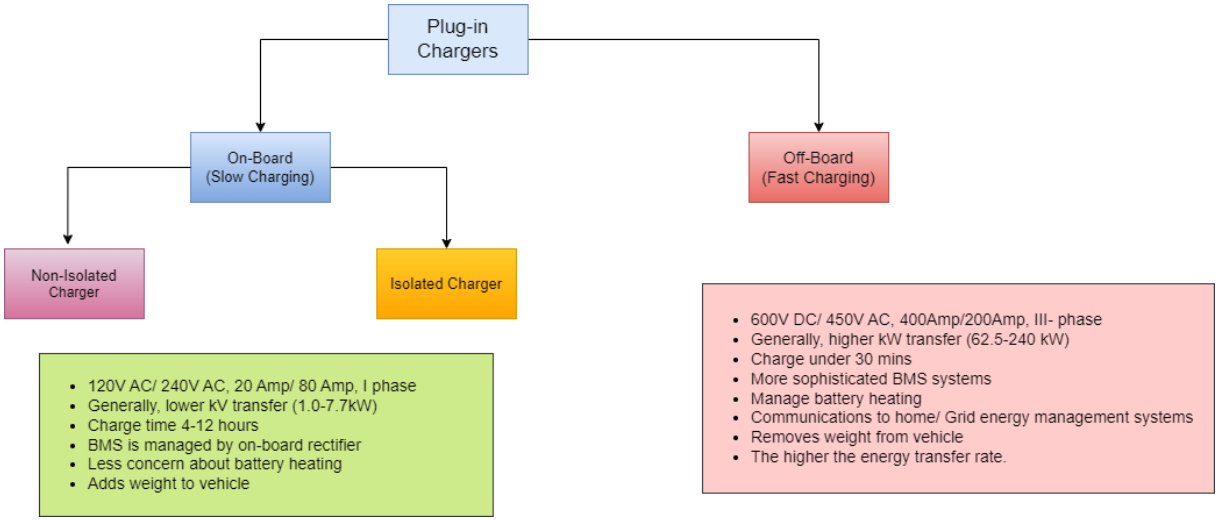

Figure 6.2: Classification of plug-in chargers.

Total harmonic distortion for current (THD_I)

$$THD_I = \frac{\sqrt{I_2^2 + I_3^2 + I_4^2 + \cdots + I_n^2}}{I_1} \times 100\% \tag{6.1}$$

Total harmonic distortion for voltage (THD_V)

$$THD_V = \frac{\sqrt{V_2^2 + V_3^2 + V_4^2 + \cdots + V_n^2}}{V_1} \times 100\% \tag{6.2}$$

There can be no THD_V, if there are no harmonics. At $n = 1$, the fundamental frequency voltage is represented as the rms voltage of the nth harmonic, V_n [156,157]. THD_I is zero for zero harmonics if I_n is the rms current of the nth harmonic and $n = 1$ is the fundamental current. THD_I is more significant than THD_V in microgrids with charging stations.

In 2018, the passenger carrier category dominated the market, accounting for over 95% of the market share in value. As a result, ride-hailing platforms, peer-to-peer ride-sharing services, taxi operators, and food delivery companies such as UBER and OLA are increasingly adopting the electrification of their vehicle fleets.This chapter presents a converter designed for applications such as Grid-to-Vehicle (G2V), Solar-to-Vehicle (S2V), and Vehicle-to-Vehicle (V2V), as depicted in Fig. 6.3. While the chapter discusses these applications, the focus is on providing a detailed analysis and simulation results specifically for the G2V application.

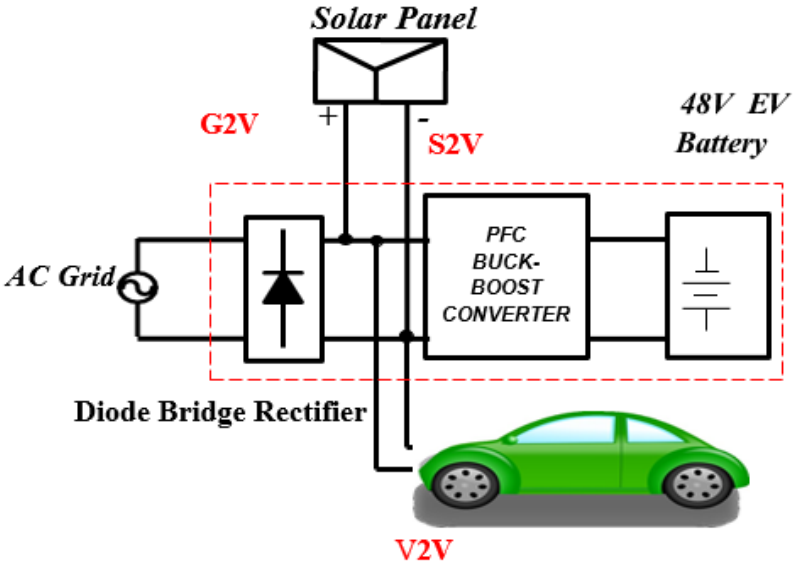

Figure 6.3: Proposed architecture for EV battery charger

6.2 Exploring Topological Options for EV Battery Chargers

The diagram in Fig. 6.3 represents the universal architecture for EV battery chargers, utilizing a single on-board converter tailored for charging batteries. The charger is capable of executing the following operations:

6.2.1 Solar-to-Vehicle (S2V)

Solar-powered vehicle charging topologies offer versatile and sustainable solutions for meeting the growing demand for electric mobility. This topology presents unique features and considerations, catering to diverse user requirements and environmental conditions. These systems reduce carbon emissions and promote a cleaner transportation ecosystem by harnessing solar energy efficiently.

While the vehicle is running or stationary and the charger is not plugged into the grid during the day, the solar panel mounted on the EVs acts as the power source, and the converter operates as a buck-boost MPPT charge controller. The ideal onboard solar power electronic topology should have a low component count to minimize size and expense and MPPT to optimize solar power output under various

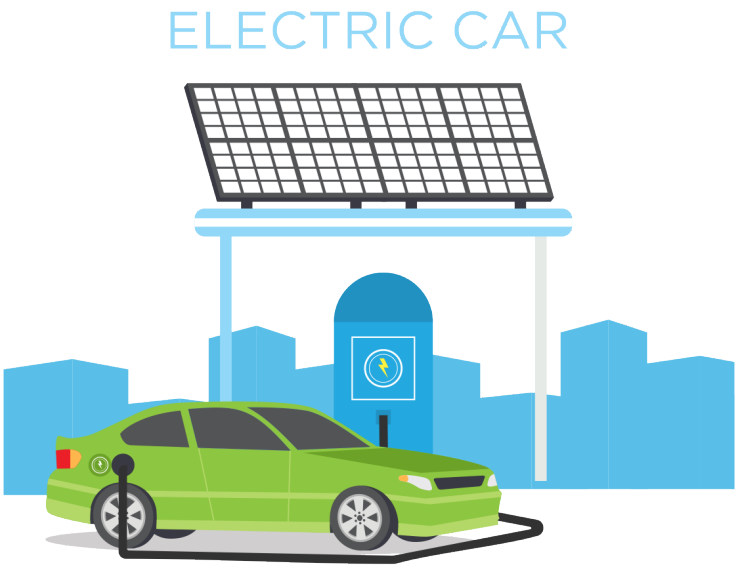

Figure 6.4: Solar-powered vehicle charging

radiation circumstances. In addition, even if the Electric car is without a solar panel, it can be charged at solar-based commercial/municipal parking and charging lots when stationary/idle, as illustrated in Fig 6.4. This charging is expected to be cheaper than grid-based charging because of the peak energy demand in the daytime supported by the local grid. The charger acts like a DC charger, as the source is DC. By employing the MPPT technique, the charger enables the EV battery to be charged with the maximum current determined by the ambient solar conditions [158].

PV Charging

PV charging involves using solar power from a PV system to charge an EV, requiring the PV array to be sized according to the number of vehicles. Charging can be achieved directly from the PV system to the EV or through an intermediate energy storage unit (ESU). The MPPT technique is vital in PV charging systems, optimizing solar energy conversion to ensure the maximum power from panels, i.e., used for battery charging. This enhances charging efficiency and speed, especially

under varying irradiance and temperature conditions. However, low solar irradiation can lead to increased Total Harmonic Distortion (THD), which is harmful to power quality, component reliability, and stability of the grid [159].

The I-V and P-V properties are also examined to implement MPPT-based EV battery charging. These variables affect the maximum available power, which changes with temperature and solar insolation levels. MPP's location will vary continuously according to irradiance and temperature, so tracking algorithms must be used to determine its location. Therefore, it becomes essential to implement MPPT techniques for the PV module. Temperature and insolation variations affect the maximum power output as well. Increased power levels indicate increased insolation, calling for a higher charging current. An efficient MPPT system must adjust to these fluctuations to guarantee the battery receives the ideal charging current.

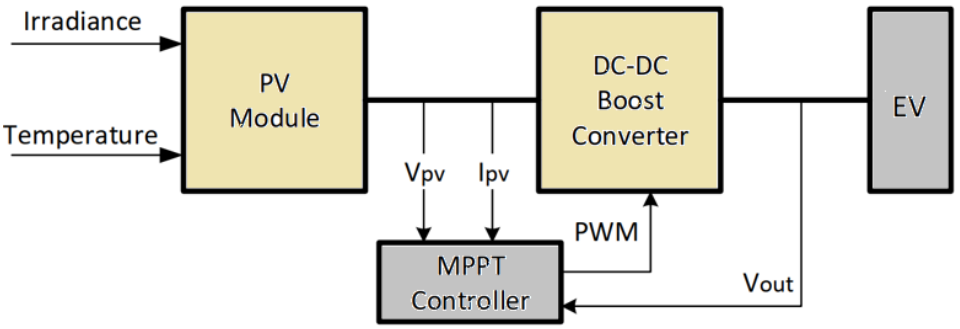

(a)

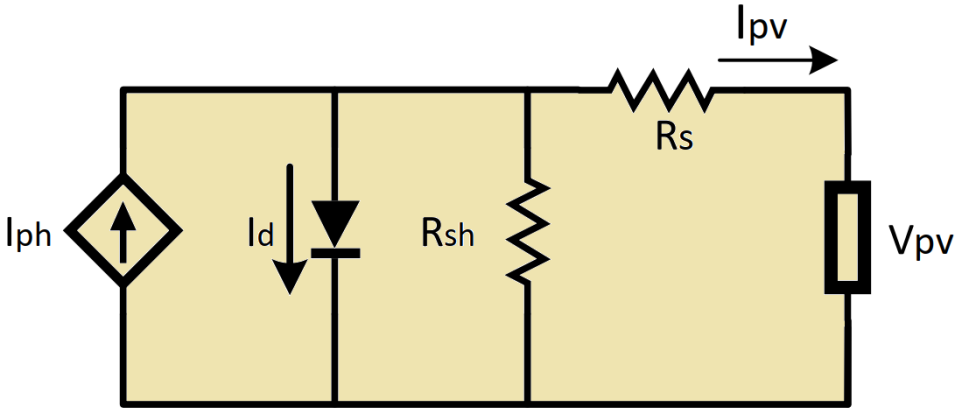

(b)

Figure 6.5: **(a)** Block diagram of MPPT controller; **(b)** A single PV module.

Fig. 6.5(a) depicts the block diagram of an MPPT controller, and Fig. 6.5(b) illus-

trates the schematic circuit of the PV module. The MPPT controller communicates with the DC-DC boost converter and provides instructions for adjusting the duty cycle to achieve the MPP based on the prevailing environmental conditions. The current-voltage (I-V) curve of a PV cell can be obtained by adjusting its voltage and measuring the resulting current to charge the EV battery [160].

6.2.2 Grid-to-Vehicle (G2V)

Adopting grid-connected plug-in EVs offers a highly sustainable approach to decreasing oil reliance and mitigating greenhouse gas emissions. However, optimizing the efficiency, convenience, and environmental impact of charging the on-board battery pack remains a significant challenge that significantly affects consumer acceptance of EVs. Power factor-corrected AC/DC converters are essential to fulfill the need for high-quality input current in PHEV battery charging. Furthermore, EV chargers, seeking heightened power density, require increased efficiency to minimize losses [161]. The pivotal performance criteria for the OBC encompass PFC, efficiency, lifetime, and cost. Displacement and distortion are two essential components of PFC, which is designed to increase the converter power factor. A Charger OBC equipped with PFC is expected to demonstrate a balance of low THD and a high PF [162, 163]. Additionally, the OBC emphasizes lifespan, primarily dictated by the component with the shortest longevity in the converter. The electrolytic capacitor is identified as the component with the least lifespan in any AC/DC switching mode power supply [164–166]. Conventional battery charger topologies exhibit deficiencies such as the absence of an active PFC unit, leading to poor THD, reduced efficiency, and increased switching and conduction losses. As a result of global inventions that facilitate technologies for transportation electrification, there has been a remarkable surge in the adoption of EVs. This growth is attributed to heightened awareness of environmental concerns and the threats posed by the depletion of fossil fuels [167].

The prevailing observation indicates that most plug-in battery chargers employ a two-stage power conversion configuration. This design, characterized by an augmented presence of semiconductor devices, results in an elevated system weight and diminished reliability. In contrast, single-stage chargers feature fewer components,

thus utilizing minimal active and passive elements. During standalone conditions, the on-board charger works in G2V mode, and battery charging is implemented with PFC to charge the 48V lead-acid batteries. The charger acts as an AC/DC active rectifier with wave shaping for PFC to produce high-quality grid current charging with UPF operation.

6.2.3 Vehicle-2-Vehicle (V2V)

EV chargers can receive power from the grid or supply power to a household via various connections, such as G2V, V2G, and V2H [168]. Moreover, EVs receive or transmit power from another vehicle through a V2V connection, as discussed in this chapter. The existing literature explores various V2V power transfer solutions, taking into account factors [35, 169], such as phases, rated power, power efficiency, circuit topologies, number of conversion stages, and other essential aspects. V2V operations are primarily classified according to the type of power transfer as depicted in Fig. 6.6. which can be AC (AC-V2V) or DC (DC-V2V). Each type involves specific conversion stages such as the number of conversion stages, phases, circuit topologies, rated power, power efficiency, and other relevant variables. V2V power transfer is implemented across three distinct power levels: Level-1, intended for slow charging (1.4-1.9 kW), Level-2, tailored for moderate charging (4-19.2 kW), and Level-3, optimized for fast charging (50-240 kW). Power electronic converters play a vital role in V2V connections, as demonstrated in Fig. 6.8, which shows various converter types used for V2V charging. The efficiency of V2V operations hinges on battery chargers, which can be either on-board or off-board chargers, as on-board chargers are classified into single-phase and three-phase chargers, recognized for their compact size, lightweight design, and cost-effectiveness [140, 170, 171]. However, off-board chargers are external fast chargers, as detailed in [172], which demand additional space.

V2V is an emergency charge transfer option and capability. V2V is becoming vital for transferring power and communication between vehicles, as demonstrated in Fig. 6.9. The proposed on-board charger can also be used in V2V mode, where one EV battery acts as a DC input source to charge a sufficient amount of the

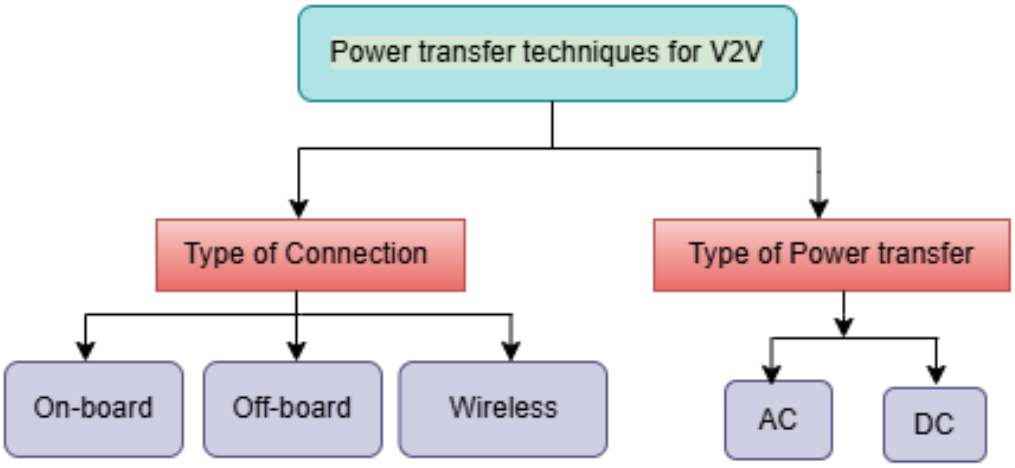

Figure 6.6: V2V power transfer classification.

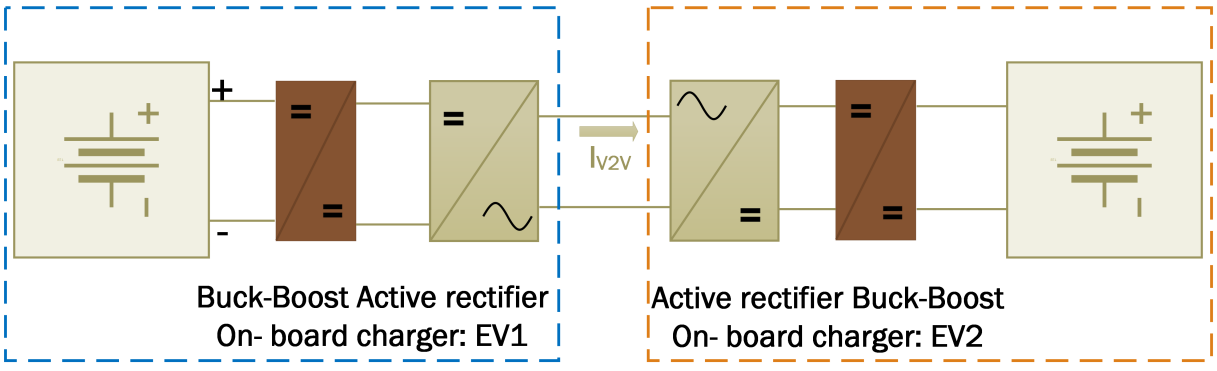

(a)

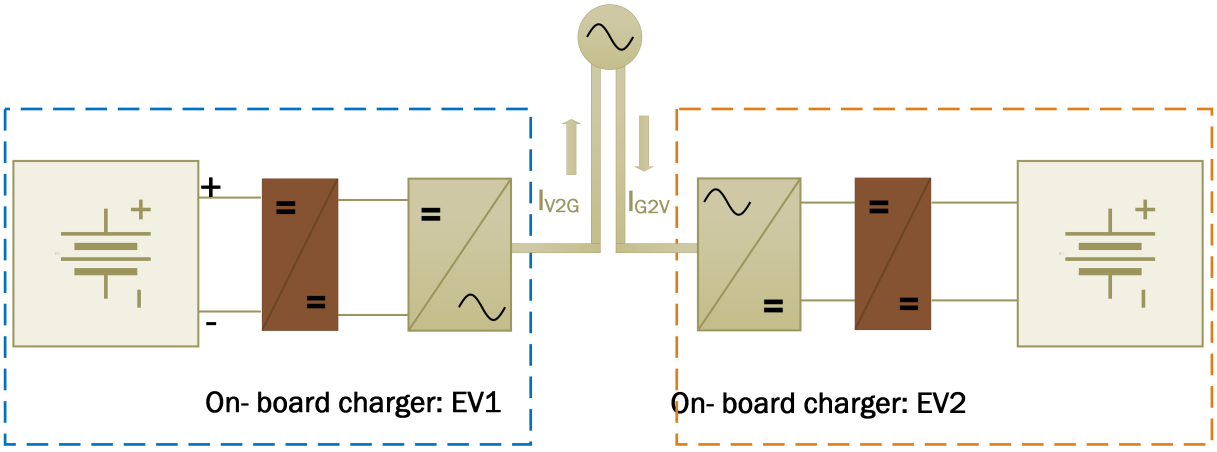

(b)

Figure 6.7: Power transfer configurations from AC to V2V: (a) on-board charger with buck-boost, (b) on-board charger grid connected.

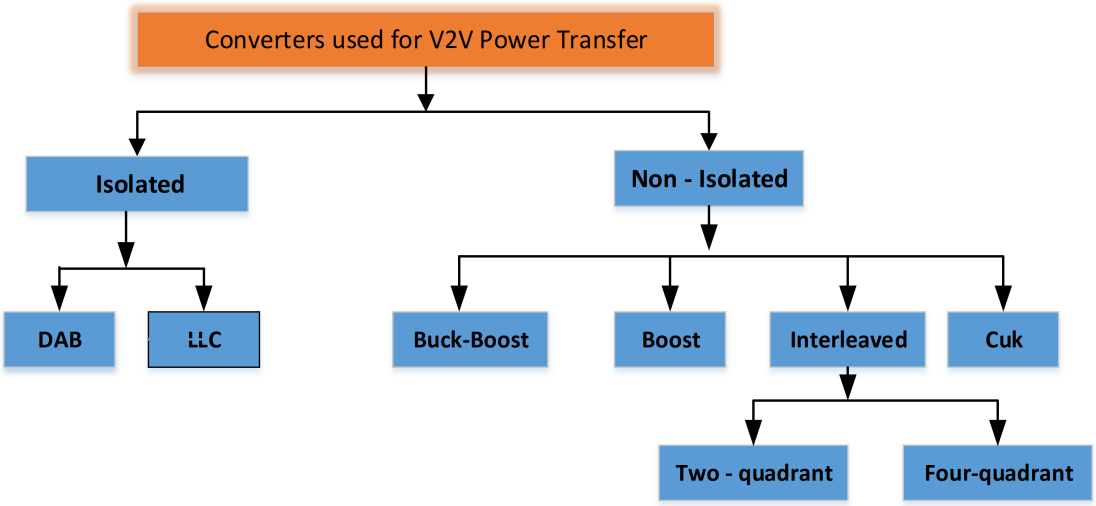

Figure 6.8: V2V Power Transfer Converters

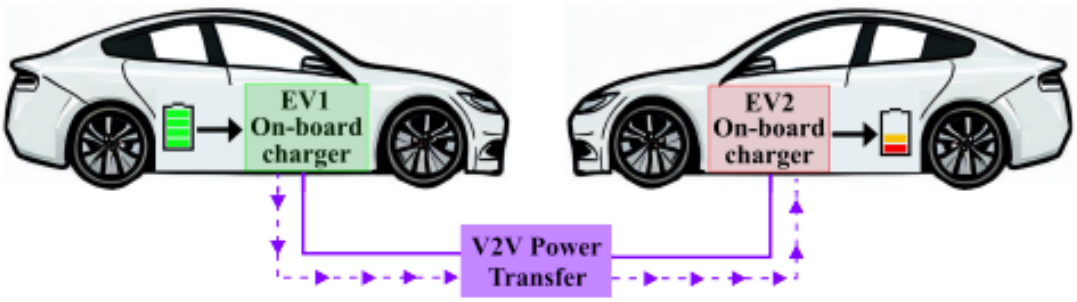

Figure 6.9: Illustration depicting V2V power transfer

other battery on another EV running out of charge to reach the charging station [173,174]. Gallium nitride (GaN) and silicon carbide (SiC) are wide bandgap (WBG) semiconductors that are becoming increasingly popular in V2V charging systems. It includes one EV acting as a source of energy via V2H to provide power to electrical loads and another EV acting as an energy recipient by using G2V. In this operational mode, the buck-boost converter is a basic DC-DC converter

Therefore, this chapter only studies and investigates G2V mode charging operation. In the literature, it is noticed that conventional grid-connected EV battery chargers are single-stage isolated DC/DC battery chargers for charging four series connected 12V, 120Ah lead-acid batteries [175]. The rising daily demand and use of EVs

affect the grid, leading to voltage distortion at the point of standard coupling due to battery chargers. Furthermore, non-isolated power converter topologies struggle with control complexity, resulting in higher input voltage currents and the need for sensors and phase-locked loop (PLL) integration [167]. Additionally, current grid-tied EV battery chargers do not incorporate the CC-CV charging mode to minimize expenses and simplify the system, as described in [176]. Battery chargers for e-rickshaws available in the market, with a power capacity of up to 1 kW, employ a straightforward charging approach by supplying a current matching the upper limit for the current of lead-acid battery [177]. The current decreases as the battery voltage rises gradually until the charging process approaches completion. This cost-effective charging method reduces the need for additional sensors and minimizes overall system complexity. In light of these considerations, a proposal has been made to use non-isolated buck-boost converters for single-cell configurations as battery chargers for e-rickshaws operating in DCM, aiming to decrease sensor count and control complexity further.

6.3 Converter Configuration and Analysis for On-Board EV Battery Chargers

On-board EV battery chargers are key to efficient energy conversion and management within the vehicle. The converter configuration impacts performance, efficiency, and reliability. OBCs typically use AC-DC converters to charge the battery, with isolated converters offering safety and non-isolated ones providing compact designs and higher efficiency. The converter features a reduced number of components, making the charger lightweight, power-dense, and cost-efficient. Its overall efficiency is high due to minimal switching losses [178]. Traditionally, non-isolated battery chargers have commonly utilized boost, buck, or buck-boost topologies to implement active PFC. This conventional design incorporates a diode bridge rectifier and established topologies to get the desired output voltage. This overview of each non-isolated topology currently in use highlights its limitations when operating in discontinuous conduction mode (DCM).

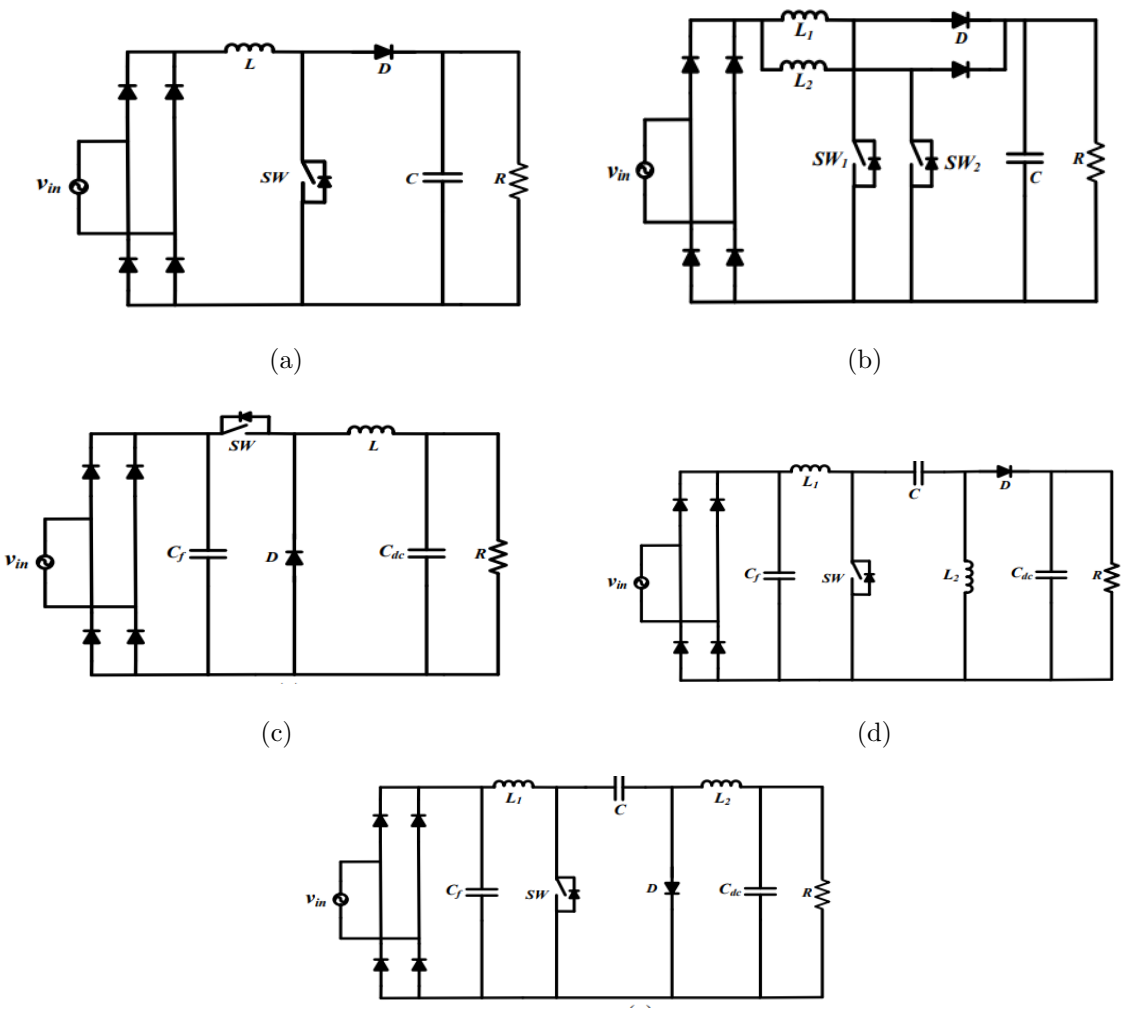

Figure 6.10: Schematic of traditional topologies ; (a) conventional boost PFC, (b) interleaved boost PFC, (c) conventional buck converter, (d) sepic converter for PFC, (e) cuk converter for PFC.

6.3.1 Conventional Boost and Interleaved Boost topology

Figs. 6.10(a) and 6.10(b) illustrate the conventional diode bridge followed by the boost and interleaved boost converter topology. It is the most widely used topology in the battery charging system as a front-end converter. A boost converter can be used for power levels up to 1 kW, while an interleaved boost converter can handle up to 3 kW. When operating in CCM, both topologies exhibit a right half-plane zero during transients, leading to unstable operation. However, when these topologies are operated in DCM, they generate odd harmonics, which can be identified through

FFT analysis of the input current, as demonstrated.

$$i_{in}(t) = \begin{cases} \dfrac{V_{DB}}{L}t, & 0 < t \leq \mathrm{t_{on}} \\ \\ \dfrac{V_{DB} - V_0}{L}t, & \mathrm{t_{on}} < t < \mathrm{T_s} \end{cases} \tag{6.3}$$

$$i_{\mathrm{in}}\,(t) = \frac{a_0}{2} + \sum_{h=1}^{\infty} \left(a_h \cos\left(h\omega_{Sw}\mathrm{t}\right) + b_h \sin\left(h\omega_{Sw}\mathrm{t}\right)\right) \tag{6.4}$$

when conducting (FFT) on the input current for a single switching cycle.

where

$$a_h = \frac{\mathrm{V_0}}{2\pi\mathrm{h}} \left(\frac{\mathrm{D}\sin(2\pi\mathrm{hD})}{L} + \frac{\cos(2\pi\mathrm{hD})}{2\pi\mathrm{h}}\right) + \frac{(V_{DB} - V_0)}{\mathrm{h}\omega_{swt}} \left(\frac{\cos(2\pi\mathrm{h})}{(2\pi\mathrm{h})2}\right) \tag{6.5}$$

$$\mathrm{b}_h = \frac{V_0}{2\pi\mathrm{h}} \left(\frac{-\mathrm{D}\sin(2\pi\mathrm{hD})}{L} + \frac{\cos(2\pi\mathrm{hD})}{2\pi\mathrm{h}}\right) - \frac{(V_{DB} - V_0)}{L} \left(\frac{\cos(2\pi\mathrm{h})}{(2\pi\mathrm{h})2}\right) \tag{6.6}$$

Where V_{DB}, V_0, and L are the rectified voltage as an input of the converter, the output voltage of the converter, and the inductor. From equation 6.5 and 6.6 it is noticed that odd harmonics are present at the input, contributing to an undesirable increase in THD. Therefore, complex control is required to achieve proper THD. Hence, this topology is not suitable for DCM-based single-stage battery chargers.

6.4 Steady-State Analysis of Interleaved Buck-Boost Converter

The interleaved buck-boost converter is an advanced power conversion topology designed to enhance efficiency, reduce current ripple, and improve transient response in power electronics applications. A DCM buck-boost becomes advantageous as the input inductor is either connected to the input or output, thus harmonics from the output are not transferred to the input side, thus achieving a good THD and unity power factor operation. It also requires fewer passive components than conventional converters, making it a more cost-effective solution for charging applications. The

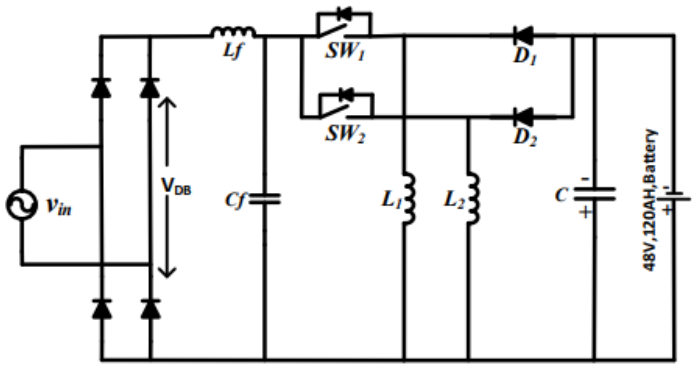

Figure 6.11: Proposed non-isolated interleaved battery charger.

Table 6.2: Specifications of proposed converter

Parameters	**Values**
Source Voltage, V_{rms}	110 V, 50Hz
Output Voltage, $V_{\mathbf{0}}$	65 V
Output Power, $P_{\mathbf{0}}$	$1KW$
Output voltage ripple, $V_{\mathbf{0}}$, ripple (t)	**5**% of output voltage ($V_{\mathbf{0}}$)
Switching frequency, f_s	50kHz
Inductance L1, L2	135μH
Capacitance	100μF

input current THD is 3.10%, which is below 5%, and the power factor is 0.9994. Therefore, the proposed converter demonstrates greater efficiency. Fig. 6.11 shows the proposed interleaved PFC buck-boost converter designed for EV batteries. Table 6.2 illustrates the Specifications of proposed converter.

This configuration combines a full bridge diode rectifier (FBDR) comprising a switch, inductor, and diode. These cells have a 180° phase shift and function at a consistent switching frequency. By operating, current stresses on power semiconductors are reduced, which improves the overall efficiency of the converter, as explained in detail [179]. It has given analysis and results for integrated buck-boost converters operating in BCM for telecom applications that use just an integrator as the controller. This chapter presents a detailed analysis of a converter in DCM for e-rickshaw charging using a PI controller, along with extensive steady-state and

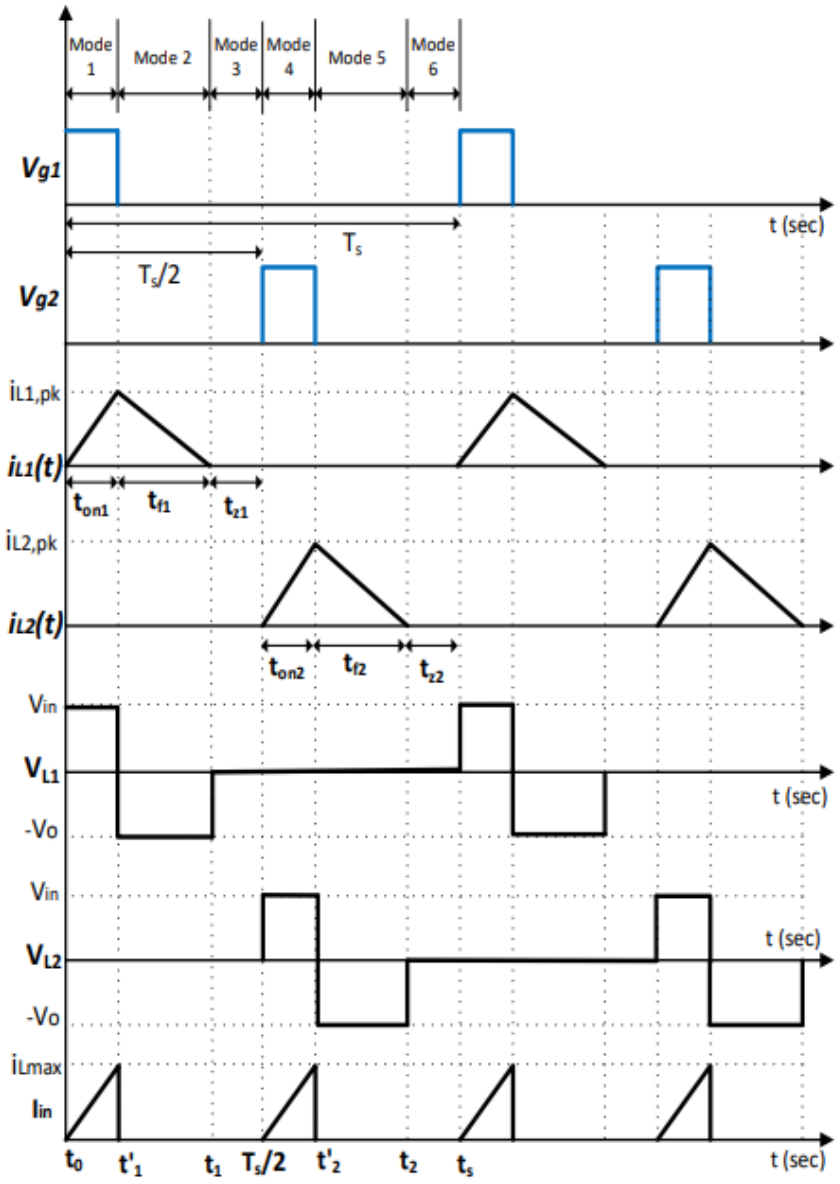

Figure 6.12: Steady-state waveform analysis of the converter.

transient results for the charger.

6.4.1 Modes of Operation

Fig. 6.12 illustrates (steady-state operation) of buck-boost for a switching cycle. These assumptions are outlined in [180, 181].

a) Ideal conditions (Zero voltage drop across semiconductors, No power losses in the system, No leakage inductance or parasitic effects in passive components) are assumed for all components.

b) Throughout a single switching period, input and output voltages are maintained at a constant level.

c) As output capacitor is adequately sized to ensure a steady output voltage.

d) As the duty cycle remains constant for a specific level.

Mode I: $0 < t < t_1{}'$

During this mode, switch SW_1 is activated, causing L_1 to charge and store energy, while capacitor C provides power to the load. Energy is not stored in L_2. The current through inductor i_{L1} is expressed as follows.

$$i_{L_1}(t) = \frac{V_{DB}}{L_1} t_1{}' \tag{6.7}$$

Mode II: $t_1' < t < t_1$

When switch SW_2 is turned off, the inductor current i_{L1} freewheels through diode D_1. Capacitor C removes ripple current, delivering a smooth DC supply to charge a battery. Now, inductor current i_{L1},

$$i_{L_1}(t) = i_{L_{1,pk}} - \frac{V_0}{L_1}(t_1) \tag{6.8}$$

Mode III: $t_1 < t < T_s/2$

In this mode, DCM operation, as The capacitor supplies the load with energy stored in L_1 that becomes zero. This time is given by,

$$t_{z_1}(t) = \frac{T_s}{2} - t_{on1} - t_{f1} \tag{6.9}$$

Mode IV: $T_s/2 < t < t_2'$

If switch SW_2 is activated, inductor L_2 charges, and capacitor C discharge as supply to load, whereas energy stored in L_2 is equal to zero. Inductor current $i_{L_2}(t)$ is

$$i_{L_2}(t) = \frac{V_{DB}}{L_2} t_2{}' \tag{6.10}$$

Mode V: $t_2{}' < t < t_2$

In this mode of operation, the gate pulse from switch SW_2 is removed. The inductor

L_2 releases its energy through the load and diode D_2, Therefore, it provides power to the load, and $i_{L_2}(t)$ is given by:

$$i_{L_2}(t) = i_{L_{2,pk}} - \frac{V_0}{L_2}(t_2) \tag{6.11}$$

Mode VI: $t_2 < t < T_s$

This is equivalent to Mode III and the DCM period specified.

$$t_{z_2} = T_s - t_{on2} - (t_{f2}) \tag{6.12}$$

6.4.2 Average current at the output

When the current delivered to load corresponds to the average diode current of both D_1 and D_2, signifying the summation of the areas under the i_{L1} and i_{L2} curves. Substituting $t = t_{f1}$ and $t = t_{f2}$ we get,

$$I_{o,\text{avg}} = \frac{1}{2} * t_{f_1} * i_{L_1,pk} + \frac{1}{2} * t_{f_2} * i_{L_2,pk} \tag{6.13}$$

where

$$t_{f1} = \frac{i_{L1,pk}}{V_0} L_1 \tag{6.14}$$

$$t_{f2} = \frac{i_{L2,pk}}{V_0} L_2 \tag{6.15}$$

$$I_{o,avg} = \frac{1}{2} * \left(\frac{i^2_{L1,pk}}{V_0} L_1 + \frac{i^2_{L_{2,pk}}}{V_0} L_2 \right) \tag{6.16}$$

$$= \frac{V^2_{DB} T_s}{V_0} \left(\frac{D^2_{1,onL2} L_2 + D^2_{2,onL2} L_1}{L_1 L_2} \right) \tag{6.17}$$

For the line period, the average current can be approximated as

$$I_{o,avg} = \frac{1}{2\pi} \int_0^{2\pi} i_{0,\text{ avg}}\, d(\omega t) \tag{6.18}$$

$$= \frac{V^2_{DB} T_s}{4V_0} \left(\frac{D_{1,\text{ on}}\, L_2 + D^2_{2,on} L_1}{L_1 L_2} \right) \tag{6.19}$$

$$I_{o,avg} = \frac{1}{2\pi}\int_0^{2\pi} i_{0,\text{ avg}}\, d(\omega t) \tag{6.20}$$

$$= \frac{V_{DB}^2 T_s}{4V_0}\left(\frac{D_{1,\text{ on}}\, L_2 + D_{2,on}^2 L_1}{L_1 L_2}\right) \tag{6.21}$$

6.4.3 Input Current

Applying power balance and using the equation,

$$\begin{aligned} P_{in} &= P_{out} \\ i_{in}(\omega t) &= \frac{Vm\sin(\omega t)Ts}{2}\left(\frac{D_{1,on}^2 L_2 D_{2,on}^2 L_1}{L_1 L_2}\right) \end{aligned} \tag{6.22}$$

$$\begin{aligned} l_{in}(\omega t) &= I_m \sin(\omega t) \\ I_m &= \frac{V_{DB}T_s}{2V_0}\left(\frac{D_{1,on}^2 L_2 + D_{2,on}^2 L_1}{L_1 L_2}\right) \end{aligned} \tag{6.23}$$

Equations 6.22 and 6.23 provide evidence of UPF operation as the input current has a pure sinusoidal waveform and is in phase with the voltage.

6.4.4 Critical conduction parameter and the operation in DCM

In DCM operation, inequalities must hold for

$$I_0 < \Delta i_{L1} + \Delta i_{L2} \tag{6.24}$$

$$I_0 < \frac{V_{DB}Ts}{2V_0}\left(\frac{D_{1,\text{on}}L_2 + D_{2,on}L_1}{L_1 L_2}\right) \tag{6.25}$$

where

$$I_0 = \frac{D_{on}V_{DB}}{D'R} \tag{6.26}$$

$$K_{\text{crit}} > \frac{4L_1 L_2}{RT_s\,(L_1 + L_2)} \tag{6.27}$$

$K_{\text{cond}} < K_{cr}(D_{on})$

which represents a stability or performance criterion involving a candidate gain value k_{cond} and a critical gain K_{cr} with some tolerance.

$$K_{\text{crit}}\ (D_{on}) = D' \tag{6.28}$$

D_{crit} is calculated to maintain DCM for all cases. D_{crit} is a value or parameter determined to ensure that the converter operates in DCM under different conditions. Alternatively, this can be formulated for the load resistance. Thus, the equation can be represented as follows.

$$R_{\text{crit}} > \frac{4L_1L_2}{D_{\text{crit}}\,T_s\,(L_1+L_2)} \tag{6.29}$$

To maintain DCM at all times

$$t_{on1} + t_{f1} + t_{on2} + t_{f2} < T_s \tag{6.30}$$

$$D\left(1 + \frac{1}{M}\sin(\omega t)\right) < 1 \tag{6.31}$$

Where, $D = D_{on,\,\text{tot}}$ and $M = \dfrac{V_0}{V_{DB}}$ The average output current is given by

$$I_{0,\text{avg}} = \frac{\mathrm{V}_0}{\mathrm{R}} \tag{6.32}$$

$$D = M\sqrt{K_{\text{cond}}} \tag{6.33}$$

where (K_{cond}), which is defined in (33), is the conduction parameter for interleaved buck-boost. For keeping the converter operating in DCM, the critical value is given by the following equation.

$$K_{\text{crit}} = \frac{1}{2(M+1)^2} \tag{6.34}$$

6.5 Modeling and Design of the proposed System

Inductor design For PFC compliance, the inductor must operate in DCM under worst-case input voltage conditions, when the input current reaches its maximum. The computation for the inductor can be performed as demonstrated by (6.35) as

$$L < \frac{V_{DB}^2 D^2 T_s}{2P_0} \tag{6.35}$$

6.5.1 Capacitor design for output

In the PFC rectifier, harmonic components are produced at double-line frequency, and the output capacitor is designed to filter these harmonic components. This results in the dispersion of power fluctuations in input and output, as demonstrated below. As a result, power fluctuations at both the input and output are dissipated through the output capacitor of the filter, as discussed below.

$$P_c(t) = P_{ac}(t) - P_o(t) \tag{6.36}$$

$$V_0 i_c = V_s I_s \cos 2\omega t - V_0 I_0 \tag{6.37}$$

Assuming efficiency to be 100%

$$i_c(t) = \frac{\mathrm{V}_s l_s}{\mathrm{V}_0} \cos 2\omega t = I_o \cos 2\omega t \tag{6.38}$$

The expression for output voltage (ripple) is provided as follows

$$V_{0,\text{ ripple}}\,(t) = \frac{1}{C} \int i_c(t) dt \tag{6.39}$$

since putting (20) in (21),

$$V_{0,\text{ ripple}}\,(t) = -\frac{I_0 \sin 2\omega t}{2\omega C} \tag{6.40}$$

$$C = \frac{I_0}{2\omega V_{0,\text{ ripple}}} \tag{6.41}$$

6.5.2 Design of Input Filters

In DCM (buck-boost), the input current will be specified as follows

$$i_{\text{in}}(t) = \begin{cases} \frac{V_{DB}}{L}t, & 0 < t \leq t_{on} \\ 0, & t_{on} < t \leq T_s \end{cases} \tag{6.42}$$

$$a_o = \frac{V_{DB}}{L} D^2 T_s \tag{6.43}$$

$$a_h = \frac{V_{DB}}{L}\left(D\sin(2\pi hD) + \frac{1}{2h\pi}\cos(2\pi hD) - \frac{1}{2h\pi}\right) \tag{6.44}$$

$$b_h = \frac{V_{DB}}{h\omega_{sw}L}\left(\frac{\sin(2\pi hD)}{2h\pi} - D\cos(2\pi hD)\right) \tag{6.45}$$

$$\text{here, } V_{DB} = V_m \sin(\omega t) \tag{6.46}$$

Equation (42) outlines the main component of the input current, while equations (43) and (44) specify the harmonics that need to be removed. Therefore, it is essential to design a low-pass LC filter with a cutoff frequency well below the converter switching frequency. This ensures that the input current consists primarily of the fundamental component, efficiently filtering out unwanted harmonics.

6.5.3 SMALL SIGNAL CONVERTER MODEL

The current-driven equivalent circuit method is CIECA, as described in [54], which can be used to derive the small-signal model of the proposed converter. So, an approach like this involves the linearization of nonlinear segments within the circuit by incorporating the average output current during each switching cycle (denoted as $I_{0_{avg}}$) generated by nonlinear elements into linear conditions. As shown in Fig. 6.13, this technique simplifies the behavior of the circuit for small-signal analysis.

$$i_{0_{avg}} = (sC + \frac{1}{R})\hat{v_o} \tag{6.47}$$

Perturbing equation (6.16) around its steady-state operating point and applying the small-signal approximation enables further analysis of the system behavior.

$$i_{0_{avg}} = \frac{{V_{in,pk}}^2 DT_s}{LV_0}\hat{d} + \frac{V_{in,pk}D^2T_s}{LV_0}\hat{v}_{in,pk} - \frac{i_{0_{avg}}}{V_0}\hat{v_0} \tag{6.48}$$

In equation (6.47) and (6.48) and substituted by $\hat{v}_{in,pk} = 0$, transfer function can be obtained.

$$T(s) = \frac{V_0(s)}{d(s)} = \frac{2V_0}{M\sqrt{K_{cond}}(sRC + 2)} \tag{6.49}$$

The dc link voltage of the converter single-pole transfer function (6.48) is regulated by a proportional-integral (PI) controller.

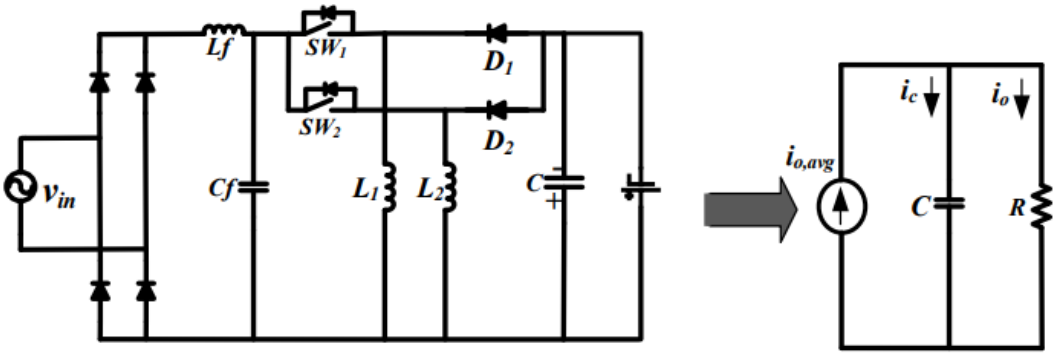

Figure 6.13: CIECA (for small signal modeling).

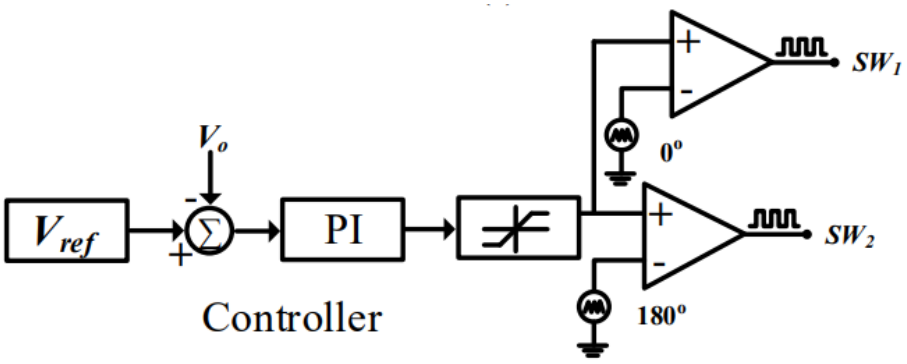

Figure 6.14: Control Scheme (Proposed Converter).

A comparison between the sensed voltage and a reference voltage is compared, and the resulting error is forwarded to a PI Controller. This PI Controller produces the d_{con} control signal. Subsequently, d_{con} is inputted into a comparator along with a

Table 6.3: assessment of proposed topology with established topologies.

Topology	N_s	N_D	N_L	***TC***	***Bidirectional operation***	***Control Complexity***	***% THD***	***Efficiency***
Converter [182]	16	0	1	17	Yes	High	2.8 %	92.57 %
Converter [183]	5	13	4	22	No	Low	6.9%	94.65 %
Converter [184]	10	4	4	18	No	Low	6.5%	95.82%
Converter [185]	10	4	2	16	Yes	Low	3%	95%
Converter [186]	12	0	3	15	Yes	Moderate	4.4%	95.1%
Converter [187]	10	4	2	16	Yes	Moderate	4.1 %	95.40%
Converter [188]	3	4	4	11	Yes	High	2.53 %	98.50%
Converter [163]	6	6	3	15	Yes	Moderate	2.08 %	92.8%
Converter [189]	12	0	2	14	Yes	Moderate	2.55 %	95.5%
Proposed converter	2	6	3	11	Yes	Low	3.10 %	96 %

No. of Switches (Ns), No. of Inductors (NL), No. of Diodes (ND), Total component count (TC)

saw-tooth signal that is phase-shifted by 180 degrees. This configuration generates pulses for the interleaving operation, as depicted in Fig. 6.14.

6.6 Result and discussion

The analysis and design of the converter have been verified by comparing simulation results, and a thorough comparison of the proposed charger is presented to highlight its superior performance compared to other topologies listed in Table 6.3. This analysis is based on various factors, efficiency, total harmonic distortion (% THD), control complexity, and the number of components utilized. From the comparison Table 6.3, it is evident that the converter designs referenced as [182], [183], [188], [189] employ a higher component count when contrasted with the proposed converter. Notably, converters [182] and [183] lack bidirectional operation capabilities and exhibit elevated THD levels from the power source while demonstrating lower efficiency than the proposed design. Although the converter [189] displays lower THD levels than the proposed one, it suffers from lower efficiency and a higher component count. Similarly, converter [188] exhibits lower THD and higher efficiency but at the expense of increased component count and greater control complexity when com-

pared with the proposed converter. The proposed converter is typically designed to operate in two stages. In the first stage, the controller functions in constant current (CC) mode, and in the second stage, it operates in constant voltage (CV) mode, depending on the SoC of the battery. A combination of logic determines the change of modes between CC and CV. If the SoC is below 80%, the EV battery charges in CC mode, and if the SoC is above 80%, it charges in CV mode, as illustrated in Fig. 6.15 (flowchart).

This interleaved converter-based charger performs better than some currently available OBCs, according to analyses of component count, stress, control complexity, THD, sensor count, efficiency, and switch stresses. The proposed converter has less component count, low switching stresses, bidirectional features, less control complexity, and low THD on the input side, i.e. (<5%). Hence, the proposed converter is more effective than other compared converters. A current-injected equivalent circuit approach (CIECA) is used to control and derive the converter's output transfer function. Due to the lower no. of inductors, the order of the system is also reduced. As depicted in Table 6.3, a few interleaved topologies [182], [183], [184], [185], [186], [187], [188], [163], [189], including the proposed OBC with LLC at the back end, exhibit higher efficiency than flyback, forward, and phase shift type at light load conditions. The reduction in the number of components led to substantial savings in OBC costs. While the total THD is 3.3%, i.e. slightly higher than the 2.5% as discussed in reference [188], as illustrated in Table 6.3, this difference is minimal and will not have a significant impact on the grid.

This paper proposes a converter for applications such as G2V, S2V, and V2V. However, it specifically focuses on a detailed analysis and simulation results for the G2V application. This single converter can perform all three tasks instead of using separate converters for DC/DC S2V economical charging, V2V emergency charge transfer, and an AC/DC rectifier for grid-based AC charging. This feature provides high power density, reduced overall cost, and enhanced flexibility for EV charging. The flowchart in Fig. 6.15 illustrates an overview of the proposed converter, followed by a discussion of its future potential and areas for further development. As per the above discussion in section II, depicted in Fig. 6.3. A single proposed converter topology is designed to manage all three power flow types (G2V, S2V, V2V).

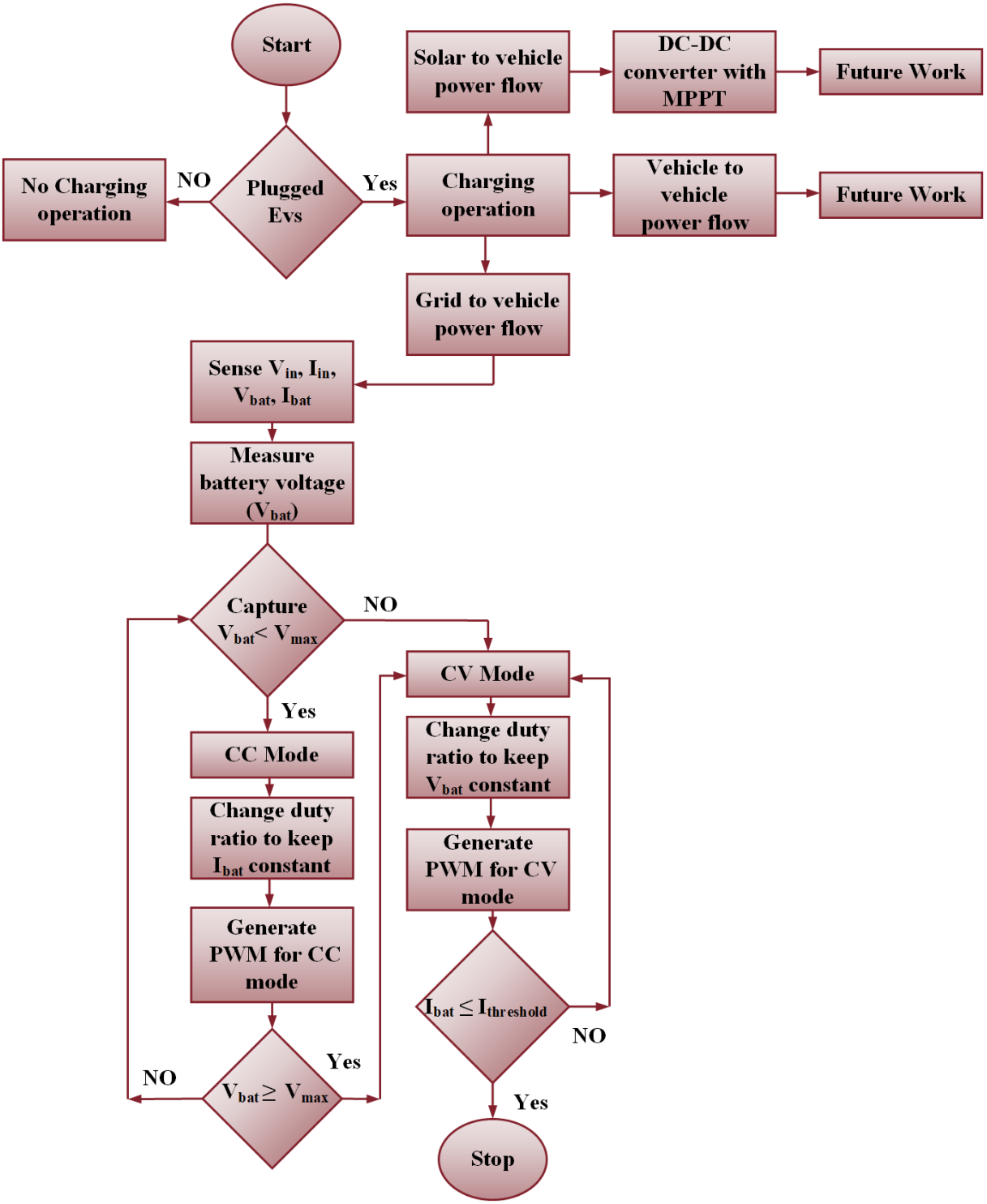

Figure 6.15: Flowchart to illustrate step-by-step processes and future work.

This involves selecting components and control strategies that adapt to input and output requirements. Future work may include the following charging techniques to improve the results of EV battery charging.

(i) S2V and V2V: Future work will include detailed analysis and simulations for S2V (with MPPT) and V2V scenarios to ensure versatility of the converter.

(ii) Grid Stability: Further studies could investigate the impact of large-scale deployment on grid stability and propose solutions for any identified issues.

(iii) Adaptive Control Strategies: Developing adaptive control algorithms that dynamically adjust to different power flow conditions in real time will enhance performance and reliability.

(iv) Machine Learning: After implementing machine learning techniques for predictive maintenance and performance optimization could improve efficiency.

6.7 Simulation results

This section aims to show the performance of the designed converter in G2V mode in the presence of disturbances, as demonstrated in Fig. 6.25 and Fig. 6.26. The simulation results show the battery side waveform as the charging voltage is 65 volts and the charging current is nearly 15 ampere. So, a 65 volt charging voltage is selected to charge a 48-volt battery, and a 15 amp charging current demonstrates charging 1 kW power. So, it is very clear from Fig. 6.19 that voltage and current at the output of the converter are DC, while Fig. 6.18 shows the current drawn from the grid side is AC with unity power factor with low THD.

This section also shows simulation results (using PSIM-11.1) of the proposed battery charger performance. The converter is configured per the outlined specifications, with the specific parameter design elaborated in Table 6.2. The cut-off frequency of the input LC low-pass filter is tuned to 5 kHz. The transfer function from control to output is expressed in equation 6.50 as

$$G(s) = \frac{v_0(s)}{d_{\text{con}}(s)} = \frac{498.82}{1 + 0.0124s} \tag{6.50}$$

A basic PI controller ($K_P + K_i/s$) is used in the control technique for the single-pole

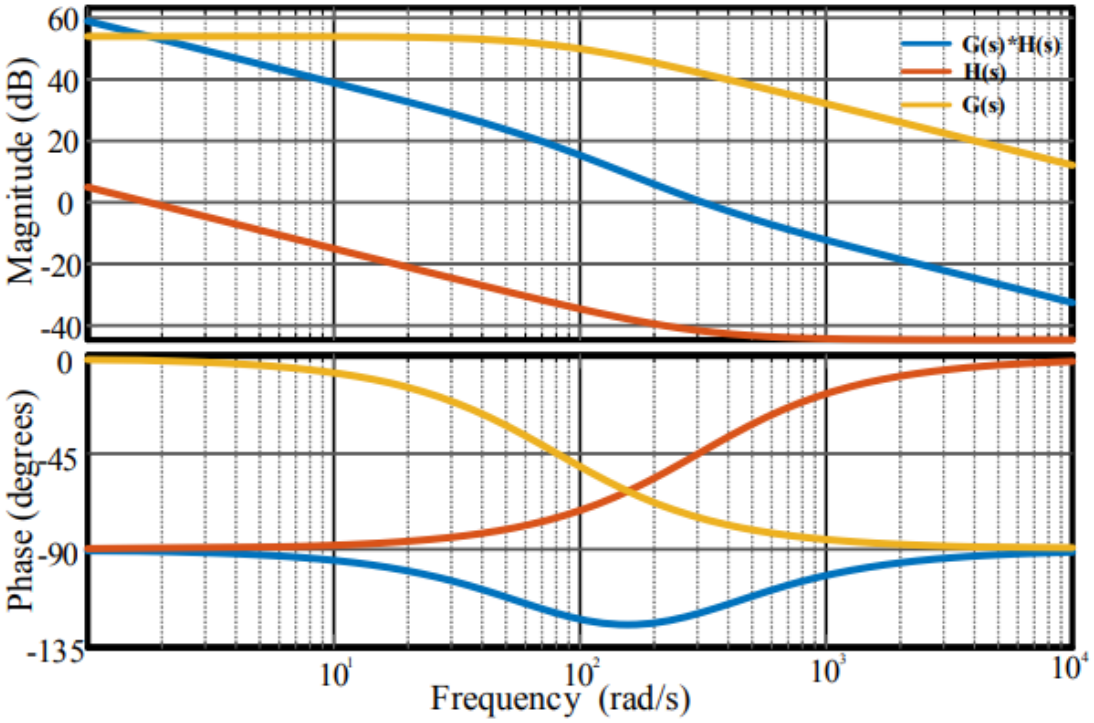

Figure 6.17: Bode Plot Comparison: G(s), H(s), G(s)*H(s).

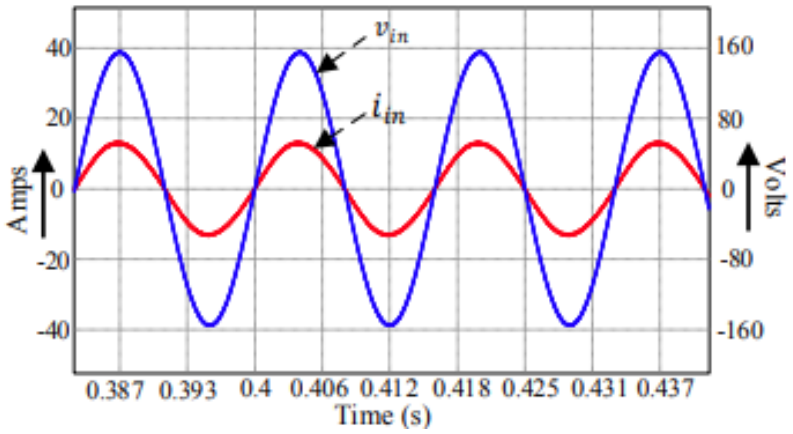

Figure 6.18: Input current and voltage waveform.

transfer function to get controlled output voltage, as demonstrated in Fig. 6.14. A PI controller with a bandwidth below 120 Hz is selected to deal with the voltage ripple in the output capacitor, which occurs at double the line frequency and ensures a 60° phase margin. Using Matlab's siso tool, this controller is fine-tuned to attain a gain crossover frequency of 314.4 rad/sec.

Fig. 6.17 illustrates the frequency response characteristics of transfer functions G(s)

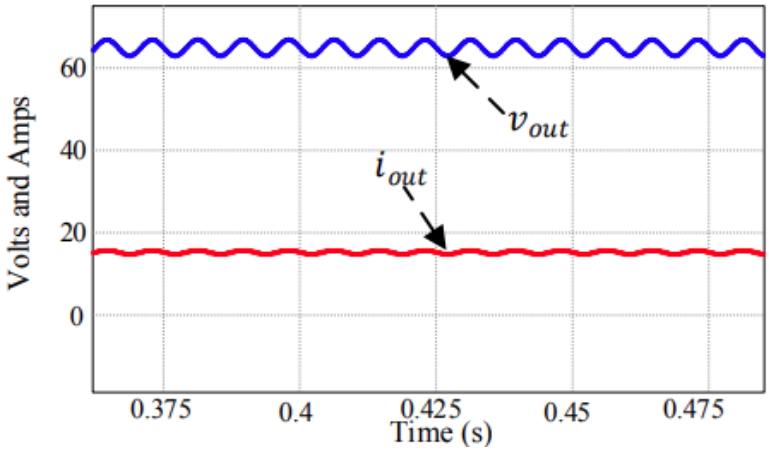

Figure 6.19: Output current and voltage waveform.

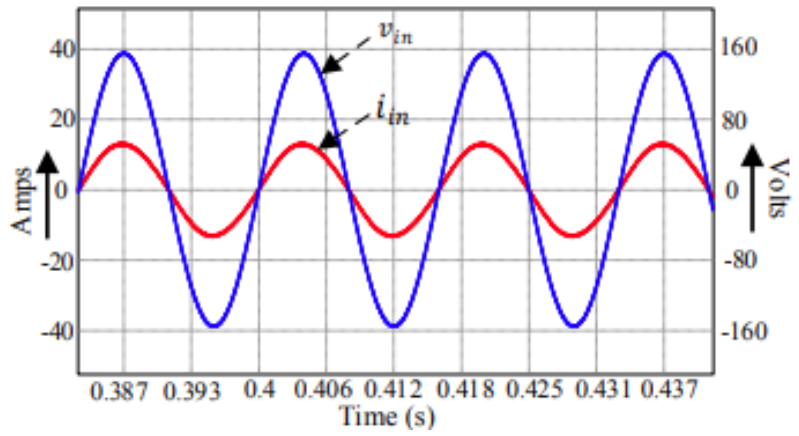

Figure 6.20: Input voltage and input current of boost PFC.

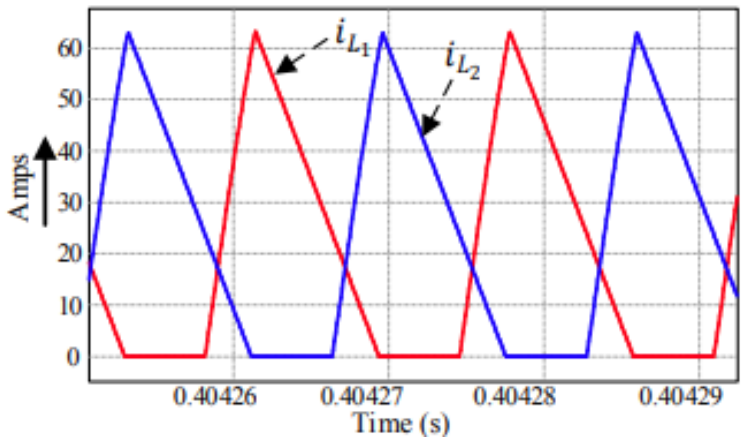

Figure 6.21: Interleaving operation waveform i_{L1} and i_{L2} in DCM mode waveforms.

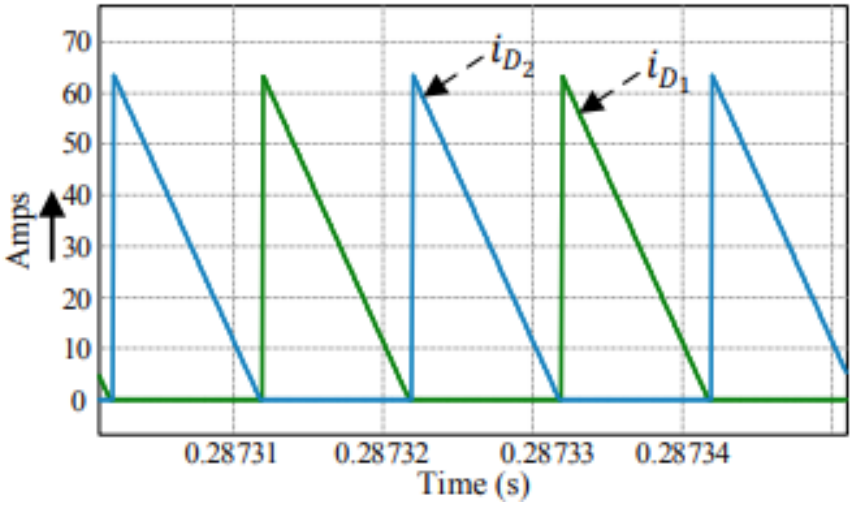

Figure 6.22: Diode current waveform i_{D1} and i_{D2}.

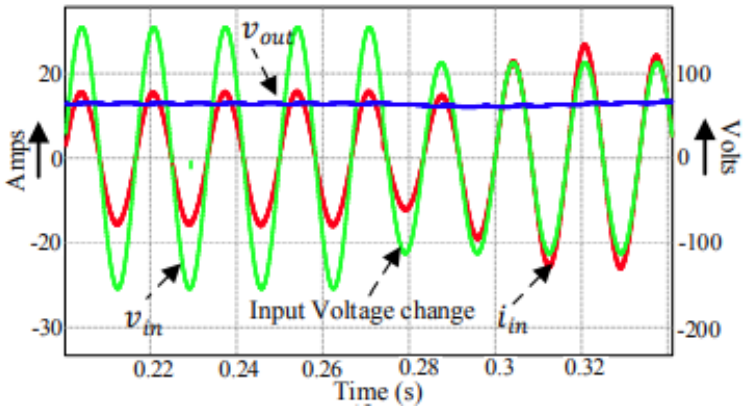

Figure 6.23: Input voltage (swell) (f) input voltage (dip).

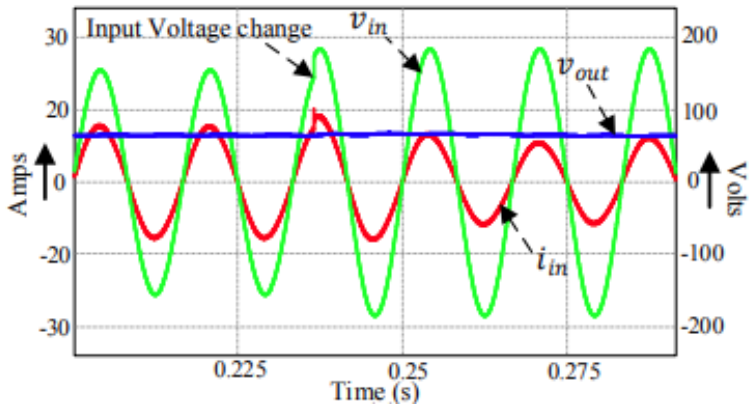

Figure 6.24: Input voltage and current waveform change.

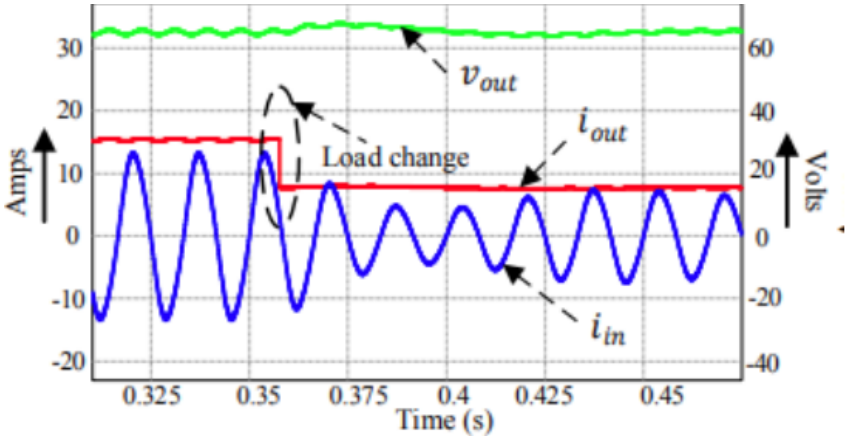

Figure 6.25: Load change (1.0 kW to 500 W).

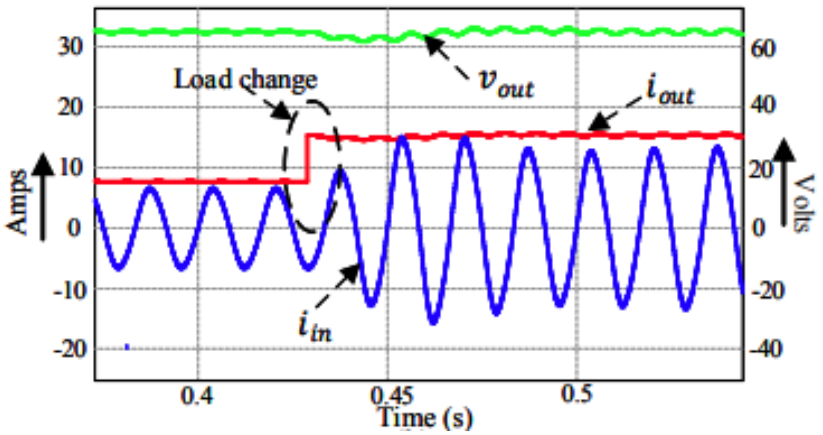

Figure 6.26: Load change (500 W to 1.0 kW).

(plant), H(s) (controller), and the open-loop transfer function G(s)*H(s). The infinite DC gain in the open loop signifies system stability for accurate tracking with zero steady-state error and robustness against disturbances in input and load. The satisfactory damping of the system is demonstrated through a 60° open-loop phase margin. The system can reject high-frequency noise with a -20 dB slope at the zero gain crossover frequency. Then, the comparator compares the sensed voltage with the reference voltage, and a resulting error is given to the PI controller. The PI controller then produces the duty cycle to regulate switches SW_1 and SW_2. A limiter is also used to control and limit the duty cycle, especially during startup and overload situations.

The results of the closed-loop simulation for the proposed converter with the designed controller are illustrated by the various figures presented in the paper. The input voltage and current waveforms of the proposed battery charger are depicted in Fig. 6.20. The input current follows a smooth, sinusoidal pattern and is in phase perfectly with the input voltage. This alignment confirms that the proposed setup operates with UPF. The output voltage and current of the single-stage charger at 1.0 kW of rated power are displayed in Fig. 6.19. The output voltage is fixed at 65 V as a reference and remains constant. Fig. 6.21 illustrates the interleaving and DCM operation of the buck-boost converter. The inductor currents exhibit discontinuity, providing validation for the design. Fig. 6.22 shows the diode current waveform of the interleaved converter. The DCM operation of the converter can be seen from the inductor current waveform shown in Fig. 6.21. Fig. 6.26 presents the converter response for a load perturbation from 50 to 100%, corresponding to an increase from 500 W to 1 kW. It has been observed that with such converters, there are zero reverse recovery losses due to the diode current being zero during this switching cycle, thereby boosting efficiency. The behavior of the converter during input voltage changes from 110V to 80V and from 110V to 130V is shown in Figs. 6.23 and 6.24, respectively. The output voltage remains nearly constant, slightly increasing and decreasing under the voltage swell and voltage dip conditions. The output voltage validates the controller design, which stays stable and closely approaches the reference voltage. Throughout the operation, the input current continuously maintains

an in-phase, sinusoidal waveform about the input voltage. Figs. 6.25 and 6.26 illustrate the converter output voltage and input current in response to the load varying from 50% to 100% and the rated power ranging from 100% to 50% Notably, output voltage precisely tracks reference voltage, achieving stability in a brief settling time of 80 ms.This outcome underscores the robustness of the controller.

6.8 Description for Interleaved Boost Converter Hardware Results:

In this experimental setup Figure 6.28, the interleaved boost converter is tested at an input voltage of 30V DC, which is stepped up to 65V DC to demonstrate its viability for EV battery charging. Figure 6.27 illustrates the hardware prototype for interleaved boost converter. The measured waveforms confirm that both inductors L_1, L_2 share the current evenly and operate in DCM, leading to reduced conduction losses and improved power quality.

6.8.1 Experimental Setup:

Complete laboratory setup for testing the interleaved boost converter, including the 30V DC power supply, the digital signal processor (DSP TMS320F28379D) for real-time control, the resistive load, and measurement instruments (oscilloscope, multimeters, etc.). The laptop is used for data acquisition and analysis of converter performance. Two inductors (L_1, L_2) and diodes (D_1, D_2) are placed on the prototyping board, along with input and output ports for connection to the DC supply and load. The design is optimized for reduced component stress and high efficiency in EV charging applications.

6.8.2 Waveform:

In the Figure 6.29 measured waveforms of the interleaved boost converter prototype operating at 30V DC input and providing a regulated 65V DC output for EV

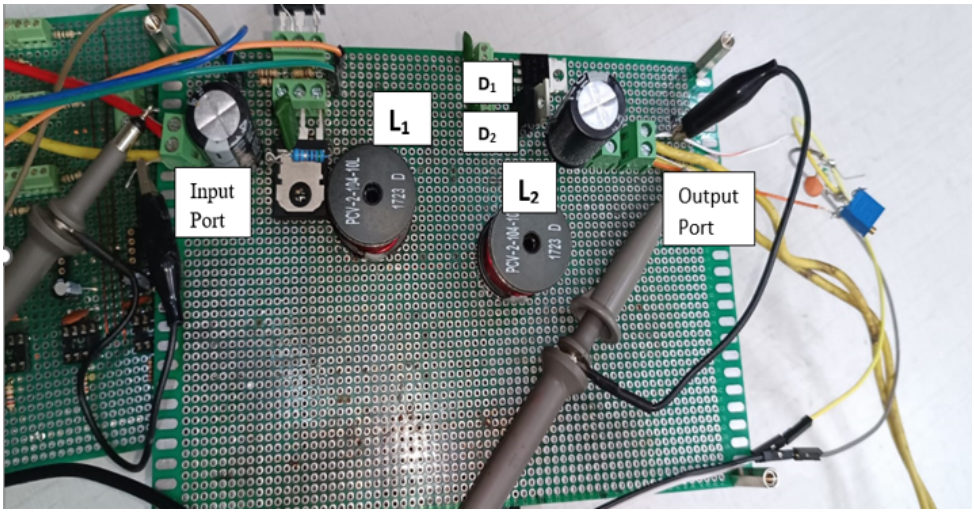

Figure 6.27: Hardware Prototype of Interleaved boost converter

.

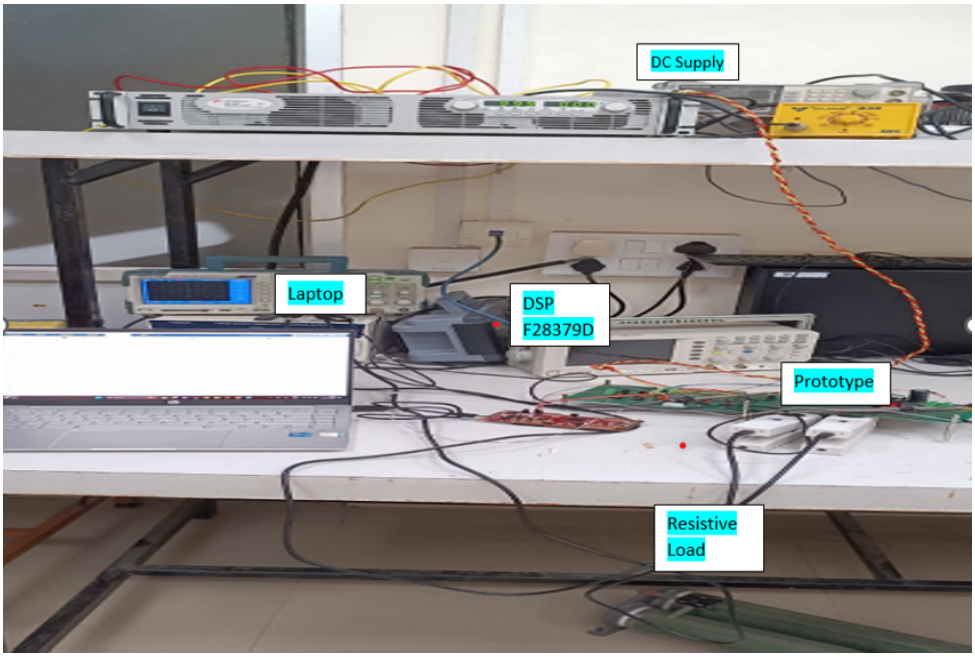

Figure 6.28: Experimental Setup.

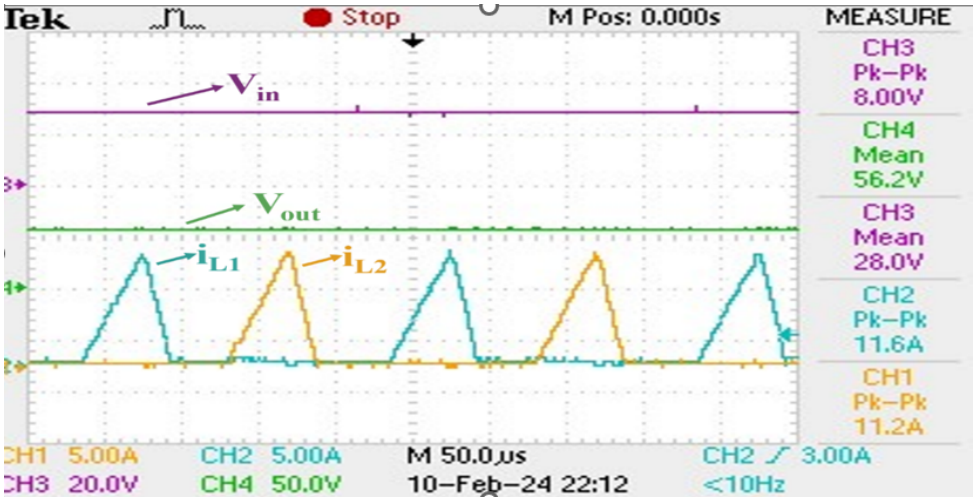

Figure 6.29: Waveform of interleaved boost converter.

charging. Channel CH_3 (purple) shows the input voltage V_{in}, while Channel CH_4 (green) indicates the output voltage V_{out}. Channels CH_1 (teal) and CH_2 (yellow) depict the inductor currents i_{L1} and i_{L2} respectively, confirming proper interleaved operation and discontinuous conduction mode (DCM).

6.9 Summary

This chapter introduced a novel interleaved buck-boost converter topology designed for AC/DC and DC/DC power conversion, particularly suited for EV battery charging. This chapter primarily focused on the detailed analysis and simulation results for the G2V application. The converter, featuring a single-sensor controller, achieved a high efficiency of 96% at 1 kW with a power factor of 0.9992 while reducing switching and reverse recovery losses. It also demonstrated effective voltage regulation with a fast settling time of 80 ms. The design was further evaluated through inductor analysis in DCM and critical conduction parameters. Its versatility extends to V2V and S2V applications, making it a promising and cost-effective solution for modern power systems.